batteries

MDPI

Article

Synergistic Effect of Redox-Active NiS-Co@C Ternary Nanocomposite for Supercapattery Hybrid Energy Storage Devices

Mohan Reddy Pallavolu [1], Jyothi Nallapureddy [2], Arghya Narayan Banerjee [2,*] and Sang-Woo Joo [2,*]

[1] School of Chemical Engineering, Yeungnam University, Gyeongsan 38541, Republic of Korea; pmreddy@yu.ac.kr
[2] School of Mechanical Engineering, Yeungnam University, Gyeongsan 38541, Republic of Korea; jyothinallapareddy@gmail.com
* Correspondence: arghya@ynu.ac.kr (A.N.B.); swjoo@yu.ac.kr (S.-W.J.)

Abstract: A highly redox-active ternary nickel sulfide and cobalt-anchored carbon nanocomposite (NiS-Co@C) electrochemical electrode is synthesized by a two-step pyrolysis-hydrothermal method using biomass-derived carbon. The high-crystalline hierarchical porous nanostructure provides abundant voids and cavities, along with a large specific surface area, to improve the interfacial properties. The as-synthesized electrode achieved a specific capacity of 640 C g^{-1} at 1 A g^{-1}, with a capacity retention of 93% over 5000 cycles, revealing outstanding electrochemical properties. Nickel sulfide nanoparticles embedded in the cobalt-anchored carbon framework improved redox activity, ion transport, and conductivity, resulting in a dominant diffusion-controlled battery-type behavior. Moreover, a hybrid supercapattery, based on battery-type NiS-Co@C as the positrode and capacitive-type activated carbon as the negatrode, achieved a maximum specific energy/power of 33 Wh kg^{-1}/7.1 kW kg^{-1} with a 91% capacity retention after 5000 cycles. The synergistic effect of the combinatorial battery–capacitor behavior of the hybrid supercapattery has improved the specific energy–power considerably, leading the development of next-generation energy storage technologies.

Keywords: cooked rice biomass; ternary NiS-Co@C nanocomposite; redox activity; battery-type behavior; hybrid supercapattery; high stability

check for updates

Academic Editor: George Zheng Chen

Received: 15 February 2025
Revised: 15 March 2025
Accepted: 19 March 2025
Published: 21 March 2025

Citation: Pallavolu, M.R.; Nallapureddy, J.; Banerjee, A.N.; Joo, S.-W. Synergistic Effect of Redox-Active NiS-Co@C Ternary Nanocomposite for Supercapattery Hybrid Energy Storage Devices. *Batteries* **2025**, *11*, 116. https://doi.org/10.3390/batteries11040116

Copyright: © 2025 by the authors. Licensee MDPI, Basel, Switzerland. This article is an open access article distributed under the terms and conditions of the Creative Commons Attribution (CC BY) license (https://creativecommons.org/licenses/by/4.0/).

1. Introduction

Supercapacitors (SCs) are essential components in modern energy storage systems, recognized for their capacity to deliver rapid bursts of power and withstand thousands of charge–discharge cycles with minimal degradation. Unlike traditional batteries, SCs store energy electrostatically, allowing for much faster charge and discharge rates, which makes them ideal for applications requiring quick energy delivery, such as in electric vehicles, regenerative braking systems, and backup power supplies. Their long cycle life and high specific power also make them suitable for use in renewable energy systems, where they can help smooth out fluctuations in energy supply. As the demand for more efficient and sustainable energy solutions grows, SCs play a key role in enhancing energy storage capabilities, improving the performance of various electronic devices, and contributing to cleaner, more reliable power sources [1,2]. However, SCs have limitations in specific energy, meaning they cannot store as much energy as traditional batteries. This makes them less suitable for applications requiring long-duration power supply. To address this, hybrid supercapacitors (HSCs) combine the advantages of SCs with those of batteries, optimizing both specific energy and power. By integrating components like lithium-ion or

other battery materials, HSCs provide a balanced solution, offering improved performance beyond electric vehicles and renewable energy systems. This advancement paves the way for an emerging field known as the supercapattery, which merges the high specific energy of batteries with the rapid charging and extended cycle life of supercapacitors, offering a superior energy storage solution in various fields, including portable electronic devices, where they extend battery life, as well as in wearable technology, off-grid storage solutions, and even hybrid transportation systems, enhancing energy efficiency and power delivery [3–9].

A high-performance hybrid supercapattery requires materials that show excellent synergy between capacitive-type surface-controlled (electric double-layer capacitance, EDLC, and pseudocapacitance, PC) and battery-type diffusion-controlled mechanisms. Nanostructured and/or carbonaceous materials with a high surface area enhance EDLC properties, while the presence of transition metal oxides/hydroxides/sulfides with abundant surface redox active sites manifest fast, reversible Faradaic redox reactions to promote PC characteristics. On the other hand, hierarchical and layered structures with plenty of voids, pores, and inter-layer spacings facilitate diffusion, enabling the intercalation/insertion of ions deep within the internal structure of the electroactive material, followed by reversible/quasi-reversible electrochemical reactions to enhance battery-type behavior. Furthermore, materials with excellent electrical conductivity (e.g., graphene, graphitic carbon with metal nanoparticles, etc.), a wide operating potential window, and strong electrochemical/mechanical/thermal stability are crucial. Chemical compatibility with electrolytes, cost-effectiveness, and eco-friendliness (such as biomass-derived carbon) are also key factors. Finally, hierarchical nanostructuring helps mitigate volume expansion during redox processes and long cycling, thereby balancing high specific energy and power with long-term durability and sustainability [10–13].

Among various transition metal oxides/hydroxides/sulfides that show both 'battery-type' and 'capacitive-type' electrochemical behaviors, nickel sulfides stand out for their cost-effectiveness, eco-friendliness, excellent electrochemical properties, and high theoretical capacitance owing to multiple redox states, structural versatility (can adopt various nanostructures like nanosheets, nanospheres, nanorods, etc.), relatively good conductivity (against other oxides/sulfides), compatibility with hybrid electrodes (can be combined with carbon materials or other conductive frameworks to improve overall performance), and thermal and chemical stability, while hierarchical morphology further enhances specific surface area, active sites, and charge transfer efficiency [14–20]. However, nickel sulfide (NiS)-based electrochemical electrodes face challenges such as significant volume expansion during redox reactions, low conductivity against carbon-based materials, dissolution in electrolytes, and aggregation of nanostructures, leading to capacity fading and poor long-term stability. Additionally, NiS has a narrow voltage window, poses potential environmental risks from sulfur byproducts, and requires complex, costly synthesis processes. Addressing these issues through structural optimization, hybridization, and electrolyte compatibility is essential to enhance their performance [12]. Apparently, compositing NiS with carbon nanomaterials like activated carbon, graphitic carbon, porous carbon, etc., prevents swelling and subsequent pulverization, enhances electron transport rate, improves high electrolyte contact areas, and increases structural stability. When metal nanoparticles are anchored onto carbonaceous materials before compositing with other electroactive materials, the functionalized carbon nanomaterials exhibit improved electron transport, increased electrolyte contact area, and enhanced structural stability, making them highly beneficial for a range of fundamental and practical applications, including electrochemical electrodes [21–23]. In this regard, a cobalt nanoparticle-anchored carbon nanostructure can

be a potential base material to fabricate a hybrid electrode due to the synergistic effect of the combination of metallic Co and graphitic carbon in alkaline medium [24].

Herein, to the best of the authors' knowledge, for the first time, we have reported a two-step pyrolysis–solvothermal method to fabricate NiS nanoparticles onto a Co-anchored graphitic carbon (Co@C) nanosheet matrix for electrochemical electrodes. The ternary NiS-Co@C nanocomposite has shown excellent battery-type electrochemical properties for hybrid supercapattery applications due to the unique morphology that provides abundant voids and cavities for reduced diffusion distances and increased reactive sites to manifest dominant diffusion-controlled processes. Additionally, the diverse oxidation states of Ni and Co, along with excess sulfur defects, have generated a significant number of redox-active sites to enhance Faradaic reactions. Furthermore, the Co-incorporated carbon matrix enhances charge–transport properties and buffers the volume expansion during long cycling to enhance stability. Therefore, the novelty of this work lies in the rational design of the morphology and the complementary integration of electrode materials to significantly boost electrochemical performance. Specifically, the synergistic combination of the battery-type behavior of NiS, the pseudocapacitive properties of Co, and the double-layer capacitance of the carbon matrix improves both diffusion-controlled and surface-controlled processes. This results in the better intercalation of electrolyte ions within the electrode's internal structure, leading to greater utilization of the active material. Consequently, the specific energy is enhanced, which is the characteristic of battery materials, while the surface-controlled process accelerates charge transfer, thus improving the specific power, which is a key feature of capacitive behavior. Therefore, the hybridization of these two electrochemical mechanisms enhances the overall energy–power performance of the ternary NiS-Co@C electrode, thus bridging the gap between supercapacitors and batteries to open up the highly important emerging field of supercapattery. In comparison to advanced commercial devices, such as Pb-acid, Ni-Cd, and Ni-MH batteries, which have specific energy values ranging from 10 to 70 Wh/kg, the current device demonstrates similar specific energy and much higher specific power. Therefore, this combination of battery and capacitor properties is crucial for addressing the power limitations of batteries and the energy constraints of supercapacitors, paving the way for the development of next-generation, highly efficient energy storage devices. Additionally, the carbon nanomaterial is derived from a biomass (cooked rice) to make the synthesis process simple, cost-effective, and compatible with sustainable development. In many households across Asia, West Africa, and Latin America, rice is a staple food, making cooked rice a significant component of food waste. Converting this bio-waste into energy materials presents a valuable opportunity for both bio-waste management and advancing sustainable development goals. Instead of relying on other biomass sources, wasted cooked rice has been chosen as the carbon precursor due to its abundant availability in households and alignment with the core principles of "*Reduce, Reuse, and Recycle*".

2. Experimental

2.1. Materials

The materials used in this study, such as nickel chloride, cobalt chloride, thioacetamide, activated carbon, NMP, PVDF, nickel foam, and potassium hydroxide, were directly used without any modifications. All chemicals were sourced from Sigma-Aldrich (St. Louis, MO, USA). The carbon source of biomass (cooked rice) was obtained from home.

2.2. Method

The methodology of synthesis includes mainly two-step pyrolysis–hydrothermal treatment. Before pyrolysis, the $CoCl_2$ (2 mM) metal precursor was first dissolved in 10 mL

of water. Then, dried cooked rice was added to the mixer to fully absorb the metallic water, which was further dried at 100 °C for 5 h. The dried product was pyrolyzed at 800 °C in a N_2 atmosphere for 2 h to obtain the Co nanoparticle-encapsulated porous carbon. This Co@C powder was further transferred to the mixer of Ni and thioacetamide precursors with a ratio of 1:1. The solution was then transferred to the Teflon-coated autoclave and maintained a hydrothermal temperature of 180 °C for 10 h. After completion of hydrothermal treatment, the resulting product was rinsed with water and ethanol multiple times, then dried at 70 °C for 8 h. The obtained NiS-Co nanosheet-nanoparticle-encapsulated porous carbon was used for characterizations and electrochemical studies. The total process is schematically presented in Scheme 1, shown below.

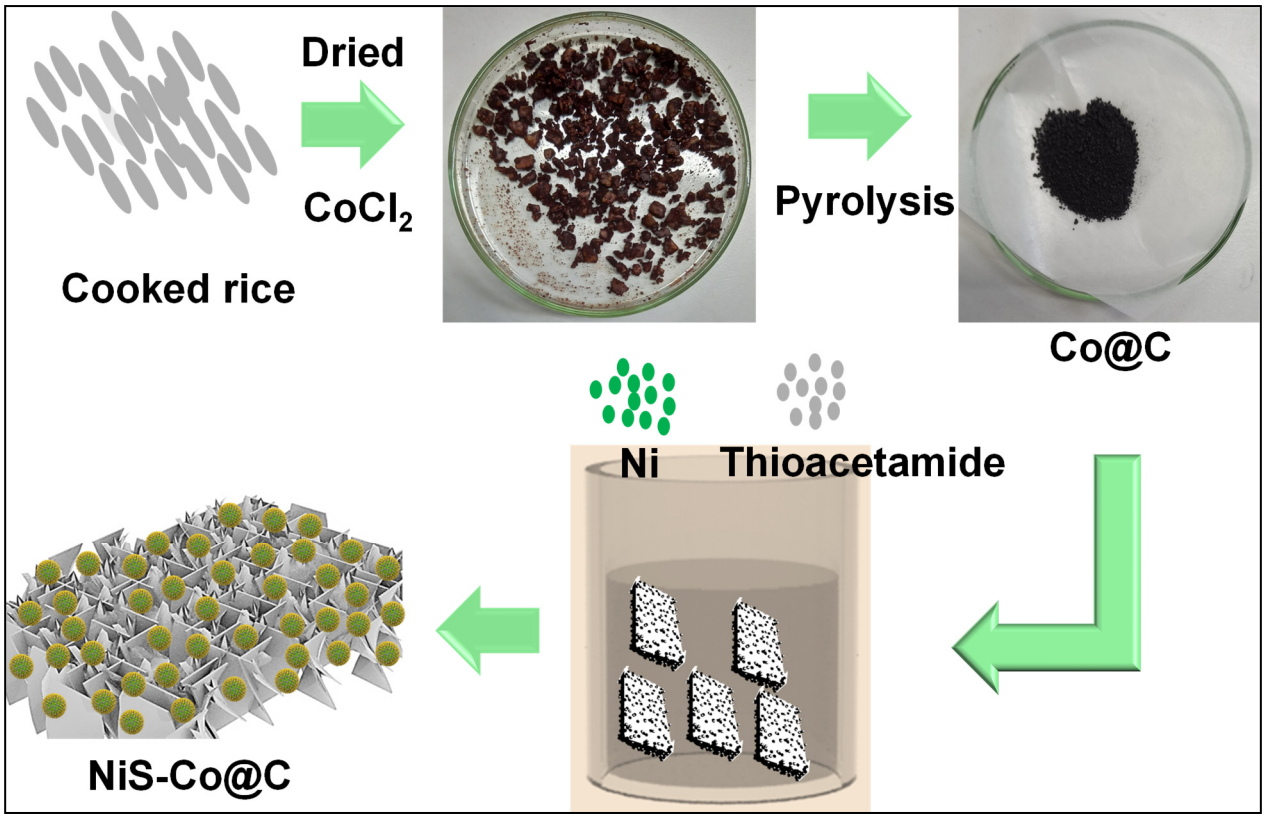

Scheme 1. Illustration of the synthesis steps of NiS-Co@C nanocomposite.

For comparison, pristine NiS nanoparticles, NiS nanoparticles deposited onto a carbon matrix (NiS@C), and Co nanoparticle-anchored carbon (Co@C) were also prepared using similar methods. These materials, along with cooked-rice-derived carbon, were further used to fabricate electrochemical electrodes. Their characteristics were then compared and correlated to evaluate the overall performance of the NiS-Co@C ternary electrode. The physicochemical and electrochemical properties, along with device fabrication parameters, are presented in the Supplementary data (S1, S2, and S3).

3. Results and Discussion

3.1. Physicochemical Properties

3.1.1. XRD Analysis

Crystallographic properties of the NiS-Co@C and Co@C samples are presented via powder X-ray diffraction (XRD) patterns in Figure 1a. For the Co@C sample (blue curve), peaks of metallic Co are observed, which correspond to the (111), (200), and (220) reflections of face-centered cubic (*fcc*)-Co (Joint Committee on Powder Diffraction Standards, JCPDS

#089-4307). Additionally, a small peak at 26° of 2θ is observed, which belongs to the (002) reflection of graphitic carbon (JCPDS #089-8487). No other oxide peaks are observed. For the NiS-Co@C sample (red curve), rhombohedral NiS peaks are observed (JCPDS #012-0041), along with metallic *fcc* Co (denoted by *) and graphitic carbon (denoted by **) peaks, indicating that the Co@C matrix is mainly acting as a conducting base to improve the overall charge–transport properties of the ternary composite for enhanced electrochemical properties [16,17,19,25,26].

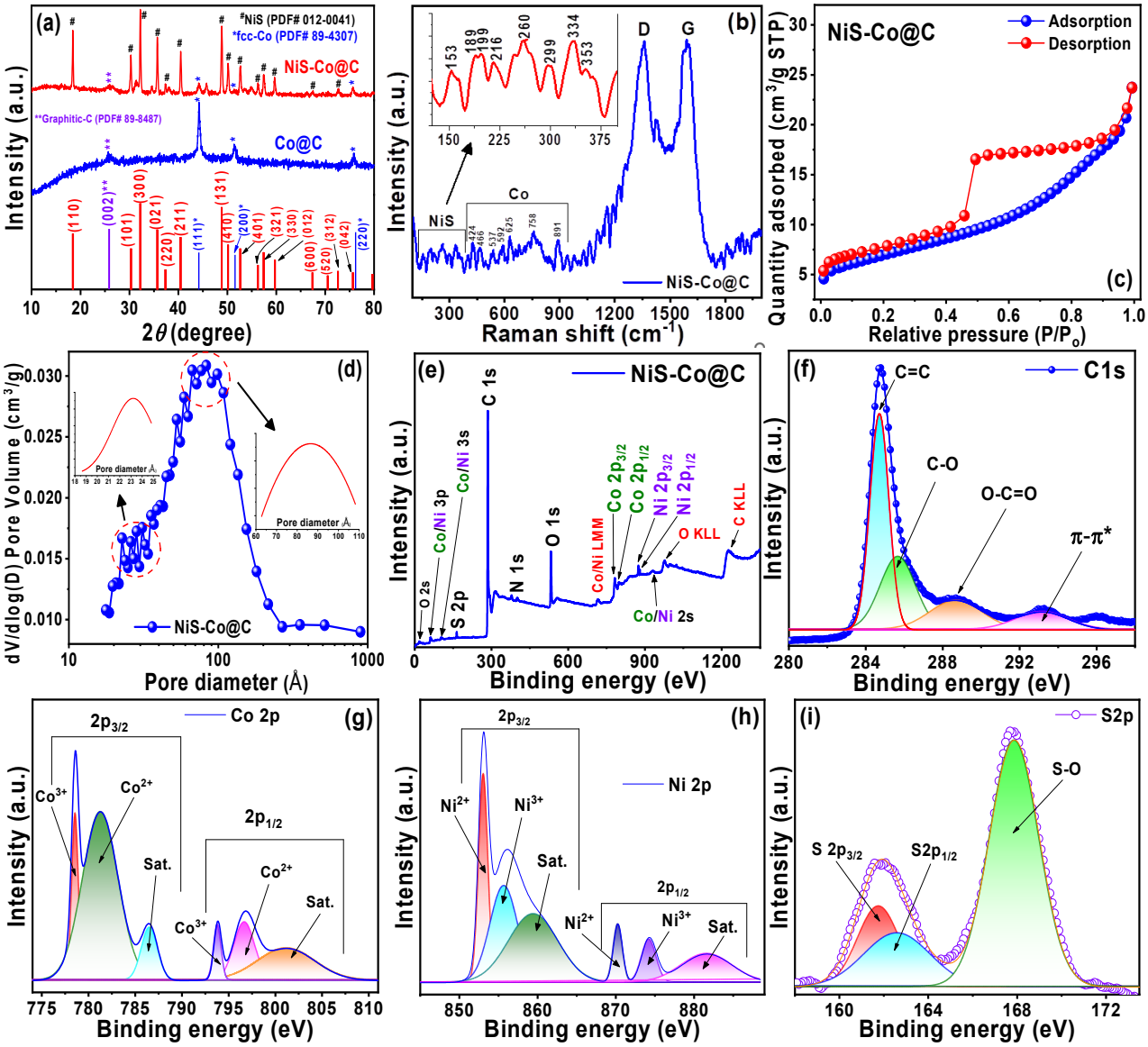

Figure 1. (**a**) XRD, (**b**) Raman, (**c**) N_2 adsorption-desorption, (**d**) pore size distribution, (**e**) XPS survey spectrum, (**f**) core level C 1s, (**g**) Co 2p, (**h**) Ni 2p, and (**i**) S 2p spectrum.

3.1.2. Raman Analysis

The Raman spectrum of the NiS-Co@C sample, shown in Figure 1b, exhibits the defect-related D peak (~1360 cm^{-1}) and the graphitic G peak (~1591 cm^{-1}). The G peak corresponds to the first order scattering of sp^2 carbon atoms caused by E_{2g} stretching vibrational modes, whereas the D peak signifies scattering induced by defects within the aromatic structure of the sp^3 bonded carbon matrix. The I_D/I_G intensity ratio provides an indication of graphitization and structural disorder, allowing the estimation of the average in-plane crystallite size (L_a) of the sp^2 domains using the relation $I_D/I_G = 102/L_a^2$ [27].

An I_D/I_G ratio less than one signifies a higher graphitic phase, while a ratio greater than one indicates increased structural disorder. In the current case, the I_D/I_G ratio is found to be 0.99 with $L_a \approx 10$ nm, indicating the formation of disordered nanographitic carbon. Raman-active peaks of Co and NiS are observed in the low energy regions. Peaks around 400 to 600 cm^{-1} are Co-related F_{2g}, E_g, and A_{1g} modes of vibrations, originating from surface oxides, which are formed during the preparation and handling of the sample. It is noteworthy that these oxides are too little to be detected in the XRD, and hence, only XRD peaks of metallic Co are observed there (cf. Figure 1a). However, Raman spectroscopy is a powerful analytical technique that mainly deals with the surface-bound local vibrational modes, crystallinity, and chemical composition of the samples, and therefore, its sensitivity is very high to detect the local oxidation states of the material. The peak at 758 cm^{-1} is due to the A_{1g} vibration mode of Co@C, while the peak at 891 cm^{-1} probably originates from the Co–Ni bonding within the NiS-Co@C ternary composite. The peaks around 100 to 400 cm^{-1} (inset of Figure 1b) are β-NiS-related vibrational modes. Eight vibrational modes are observed, which is in agreement with the literature values. However, some vibrational modes may not be detectable, or they may shift slightly. This could be attributed to the size effect of the nanomaterials, as Raman vibrational modes are highly sensitive to the vibrations of the crystal lattice. When the crystal size is scaled down to the nanoscale, the atomic arrangement within the lattice may vary from that of bulk materials, which can influence the vibrational modes [26,28–33].

3.1.3. BET-BJH Analysis

Figure 1c,d presents the N_2 adsorption/desorption isotherms and pore size distributions for NiS-Co@C, respectively. The graph in Figure 1c shows a characteristic type IV N_2 adsorption–desorption isotherm, featuring a distinct H2-type hysteresis loop within the relative pressure range of 0.42 to 0.94. This behavior suggests that the material possesses a mesoporous structure with a narrow mesopore size distribution. Additionally, the steep slope above 0.94 and the gradual slope below 0.42 suggest the presence of macropores and micropores within the nanosheets as well. The pore size distribution, shown in Figure 1d, spans from 1.7 to 100 nm, with two preponderances at 1.8–2.5 nm and 6.0–11.0 nm (shown at the insets), further substantiating the presence of both micropores and mesopores. The Brunauer–Emmett–Teller (BET) specific surface area and Barrett–Joyner–Halenda (BJH) pore volume are found to be about 24.15 m^2/g and 0.034 cm^3/g, respectively. On the other hand, the N_2 adsorption–desorption and pore size distribution of the Co@C sample are shown in Figure S1. The adsorption–desorption graph (Figure S1a) exhibits the Type-II isotherm, which is typical of macroporous or non-porous structures. Additionally, a small type-H4 hysteresis loop is observed, indicating the presence of a small amount of micropores and mesopores as well. The pore size distribution (Figure S1b) shows a small peak near the micro-to-mesoporous region, indicating the presence of small amounts of micropores and mesopores within the predominant macroporous or nonporous structure. The BET specific surface area and BJH pore volume are found to be about 8.0 m^2/g and 0.047 cm^3/g, respectively. A comparison of these data with the NiS-Co@C sample indicates that the deposition of NiS nanoparticles considerably increased the BET surface area of the latter sample, while the BJH pore volume remains higher in the Co@C sample due to the presence of predominant macropores.

These results highlight the porous structure of the graphitic carbon sheets. The porous nature of the NiS-Co@C nanosheets plays a crucial role in their electrochemical performance by facilitating electrolyte diffusion, enhancing accessibility to active sites, accommodating large volume changes during ion insertion/extraction, and maintaining structural integrity.

This improves electronic conductivity, supports efficient charge transfer, and contributes to the material's excellent cycle stability [34].

3.1.4. XPS Analysis

The different oxidation states and electronic structures of the samples are revealed through X-ray photoelectron spectroscopic (XPS) measurements. The XPS survey spectra of NiS-Co@C (Figure 1e) show peaks corresponding to Ni, Co, S, C, and O in various electronic states, as well as some Auger peaks. The C 1s core-level spectrum, shown in Figure 1f, is separated into three sub-peaks that represent C=C, C-OH, and C=O bonds, along with a π–π^* satellite peak. All the peak positions, full width at half maximum (FWHMs), and the area under the peaks of the various core-level spectra for both samples are compared in Table S1. In the high-resolution Co 2p spectra of NiS-Co@C (Figure 1g), peak deconvolution identifies the Co $2p_{3/2}$ and Co $2p_{1/2}$ peaks of Co^{2+} and Co^{3+}, accompanied by strong satellite peaks from metallic ions, which are also reflected in the dominant XRD peaks of metallic Co. However, the presence of the Co^{2+} and Co^{3+} peaks in the Co 2p spectrum indicates oxide formation as well, but the absence of the corresponding XRD peaks is mostly due to their amorphous nature. The high-resolution Ni 2p spectra, shown in Figure 1h, also reveal the presence of both Ni^{3+} and Ni^{2+} oxidation states within the deconvoluted Ni $2p_{3/2}$ and $2p_{1/2}$ peaks. For both Ni 2p and Co 2p spectra, the presence of both Co^{3+}/Co^{2+} and Ni^{3+}/Ni^{2+} states is attributed to the carbonization and sulfurization processes, which generate multiple oxidation states, thereby improving redox activity. The S 2p spectrum (see Figure 1i) shows the presence of S^{2-} species, indicated by the S $2p_{3/2}$ and S $2p_{1/2}$ sub-peaks, along with a satellite peak corresponding to the S–O bond. The diverse oxidation states of Ni and Co provide rich redox activity, while the oxidation states of sulfur offer defect centers, both of which improves the electrochemical performance of the NiS-Co@C electrode, as shown later [35–37]. The corresponding peak positions, FWHM, and peak areas are compared in Table S1. It is well-known that the area under the curves in an XPS spectrum is interpreted as a measure of the relative abundance of different elements or chemical states present in the sample. As expected, C 1s contributes nearly 77% of the total area under the XPS curve, indicating the highest elemental presence, which is due to the use of the carbon matrix as the base of the NiS-Co@C nanocomposite. On the contrary, Ni 2p and Co 2p contribute 3.4% and 3.7% against the total area, indicating nearly equal elemental presences within the nanocomposite. This indicates that both nickel and cobalt equally contribute towards the redox activities to enhance the electrochemical properties of the NiS-Co@C electrode. Likewise, the contribution from S 2p is around 4.5%, revealing nonstoichiometric sulfur excess within the nanocomposite, which creates defect centers to enhance redox activities (discussed later).

3.1.5. SEM-TEM Analysis

Scanning electron microscopic (SEM) images of Co@C and NiS-Co@C samples are shown in Figure 2a–c and Figure 2d–f, respectively. Both samples feature curly shaped, highly porous hierarchical nanostructures, which, at higher magnifications, reveal 2D nanosheet-like structures, with the NiS-Co@C sample showing larger pores. In particular, the NiS-Co@C sample exhibits a uniform deposition of NiS nanoparticles within the Co@C matrix, enhancing the redox activity of the electrode for improved electrochemical performance. This is further supported by transmission electron microscopic (TEM) images of NiS-Co@C (Figure 2g–j) at four different magnifications, where the highly porous nanosheet-like structures and the NiS nanoparticle deposition are clearly visible. The size distribution of the NiS nanoparticles (shown in the inset of Figure 2h) shows a peak size of approximately 30 nm. Additionally, the high-resolution (HR) TEM micrograph in Figure 2k reveals the high-crystallinity of NiS and Co lattice planes, with well-defined lattice spacings.

Figures S2a–e and 2l show the EDX mapping/spectrum and elemental compositions of Co@C and NiS-Co@C, respectively, which reveal the uniform presence of the corresponding elements [34,38]. The compositional analyses depict that, for the NiS-Co@C sample, there is a slightly excessive sulfur incorporation (similar to XPS data), which may create defects to improve redox activity. For both the electrodes, considerable incorporation of Co indicates its positive contribution towards the electrochemical performance via enhanced redox activity as well as enhanced charge–transport properties. Additionally, the considerable presence of oxygen indicates the remnant CO_2 absorption during sample preparation and handling. The presence of Au is due to the gold-coating used on the sample for proper electron microscopic imaging. The trace amount of K in the Co@C sample is likely a result of impurities from the cooked rice, often introduced through fertilizers. However, during the hydrothermal reaction with $NiCl_2$ and thioacetamide, it was likely removed, and hence, no elemental K is observed in the NiS-Co@C sample.

3.2. Electrochemical Properties in a Three-Electrode Setup

The electrochemical performance of the NiS-Co@C and Co@C electrodes was investigated through cyclic voltammetry (CV), galvanostatic charge–discharge (GCD), and electrostatic impedance spectroscopic (EIS) measurements in a three-electrode (half-cell) setup.

3.2.1. CV Analysis

The CV curves for both electrodes at different scan rates are presented in Figures 3a and S3a. Strong anodic and cathodic peak pairs appear within the potential range of −0.1–0.6 V (vs. Ag/AgCl). Additionally, we compared the CV curve of the ternary NiS-Co@C electrode with binary Co@C (cobalt nanoparticles anchored into a carbon matrix), binary NiS@C (NiS nanoparticles deposited onto a carbon matrix), pristine NiS, and an as-prepared carbon electrode in Figure 3b (@2 mV/s scan rate), revealing broader integral area and higher peak currents of the NiS-Co@C electrode against the other electrodes, indicating its superior electrochemical performance. This clearly indicates the relative contributions of the individual components in the overall electrochemical performance of the NiS-Co@C electrode. For example, pristine NiS (the black curve in Figure 3b) depicts typical battery-type behavior with strong redox peaks but very low peak currents and minimal integral area, indicating poor electrochemical properties. On the other hand, the CV curves of the as-prepared carbon electrode (inset of Figure 3b) reveal typical quasi-rectangular shapes of EDLC behavior. Nevertheless, the current is observed to be very low, indicating its inferior electrochemical performance. However, when the pristine NiS nanoparticles are deposited onto the as-prepared carbon matrix to fabricate the NiS@C electrode (the green curve in Figure 3b), both peak currents and integral area are found to be increased. This indicates that the battery-type redox activity of NiS is combined with the EDLC behavior of carbon to enhance the overall electrochemical activity of the binary NiS@C electrode. Likewise, the anchoring of the redox-active cobalt nanoparticles with the double-layer capacitive carbon leads to the enhanced supercapacitive performance of the binary Co@C electrode (the blue curve in Figure 3b). Hence, the hybridization of all these components into the ternary NiS-Co@C electrode manifests the combinatorial effect of the redox behavior of NiS, Co, and EDLC properties of the carbon matrix to considerably enhance the overall electrochemical performance of the NiS-Co@C composite electrode (the red curve in Figure 3b). Evidently, this enhancement can be attributed to the presence of the diverse oxidation states of Ni and Co (e.g., Ni^{2+}/Ni^{3+}, Co^{2+}/Co^{3+}) in the NiS-Co@C sample, which promote more extensive and faster redox activity compared to Co@C. Furthermore, the NiS-Co@C electrode benefits from the presence of sulfide ions that introduce additional defects and form larger voids/pores (shown in Figure 2), which provide more surface-active sites to further enhance the redox activity compared to Co@C. The CV curves of both elec-

trodes show pronounced redox peaks during the anodic and cathodic sweeps, suggesting that Faradaic redox reactions occur during charge/discharge cycles, involving the valence changes of Ni^{2+}/Ni^{3+} and $Co^{2+}/Co^{3+}/Co^{4+}$. For example, in the CV curve of the NiS-Co@C electrode (at a scan rate of 2 mV/s), the anodic peak at 0.40 V and cathodic peak at 0.17 V indicate typical battery-type behavior for the Ni^{2+}/Ni^{3+} conversion, corresponding to the following reversible Faradaic reaction [17,38]:

$$NiS + OH^- \leftrightarrow NiSOH + e^- \quad (1)$$

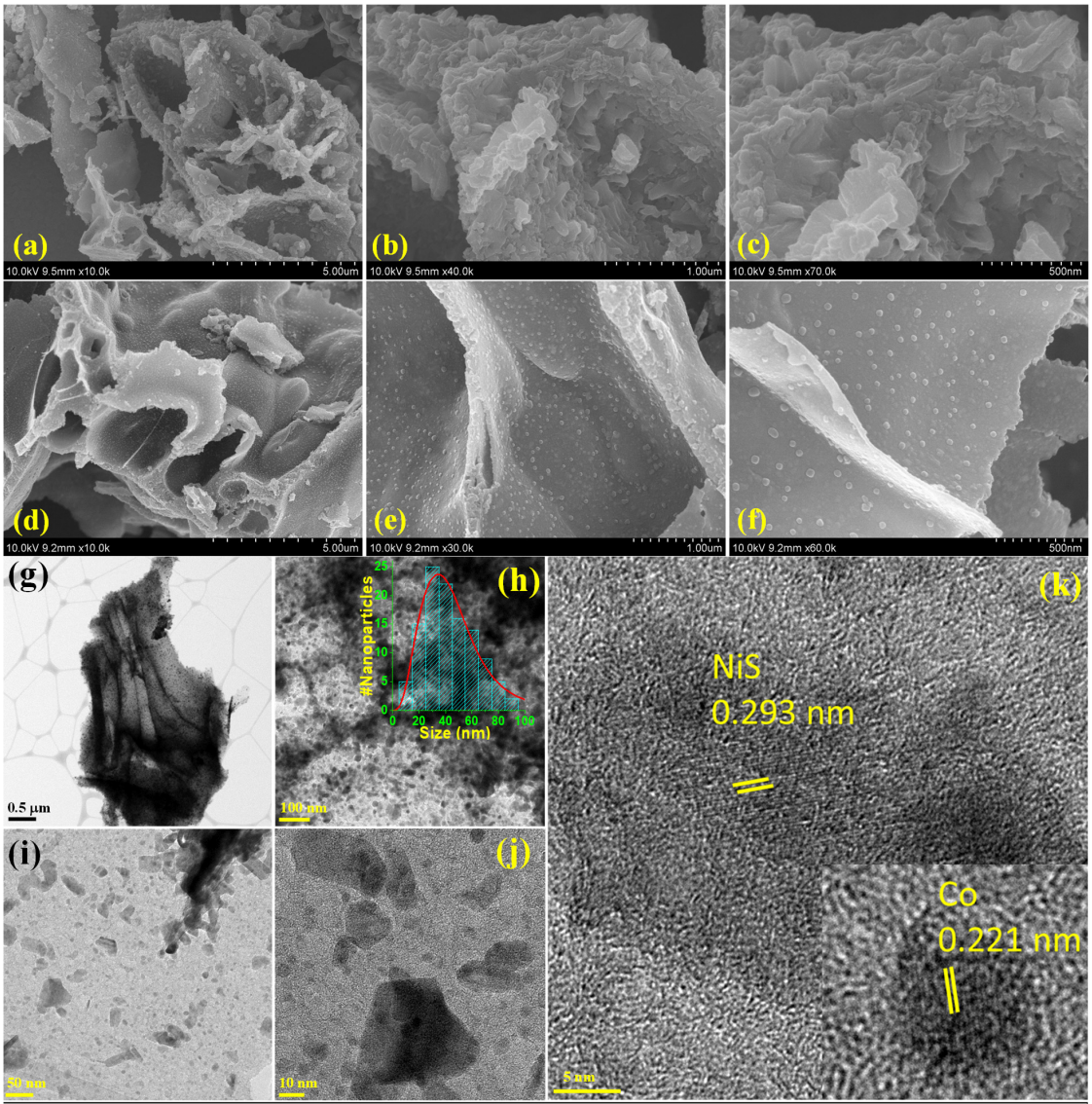

Element	Wt%	Atomic%
C	47.51	70.98
O	16.35	18.34
S	7.15	4.00
Co	7.84	2.39
Ni	11.00	3.36
Au	10.15	0.92
Total	100.00	100.00

Figure 2. (**a**–**c**) SEM images of Co@C, (**d**–**f**) NiS-Co@C (at three magnifications), (**g**–**j**) TEM images of NiS-Co@C (at four magnifications) (inset of h: size distribution), (**k**) HRTEM, (**l**) EDX of NiS-Co@C, and elemental composition.

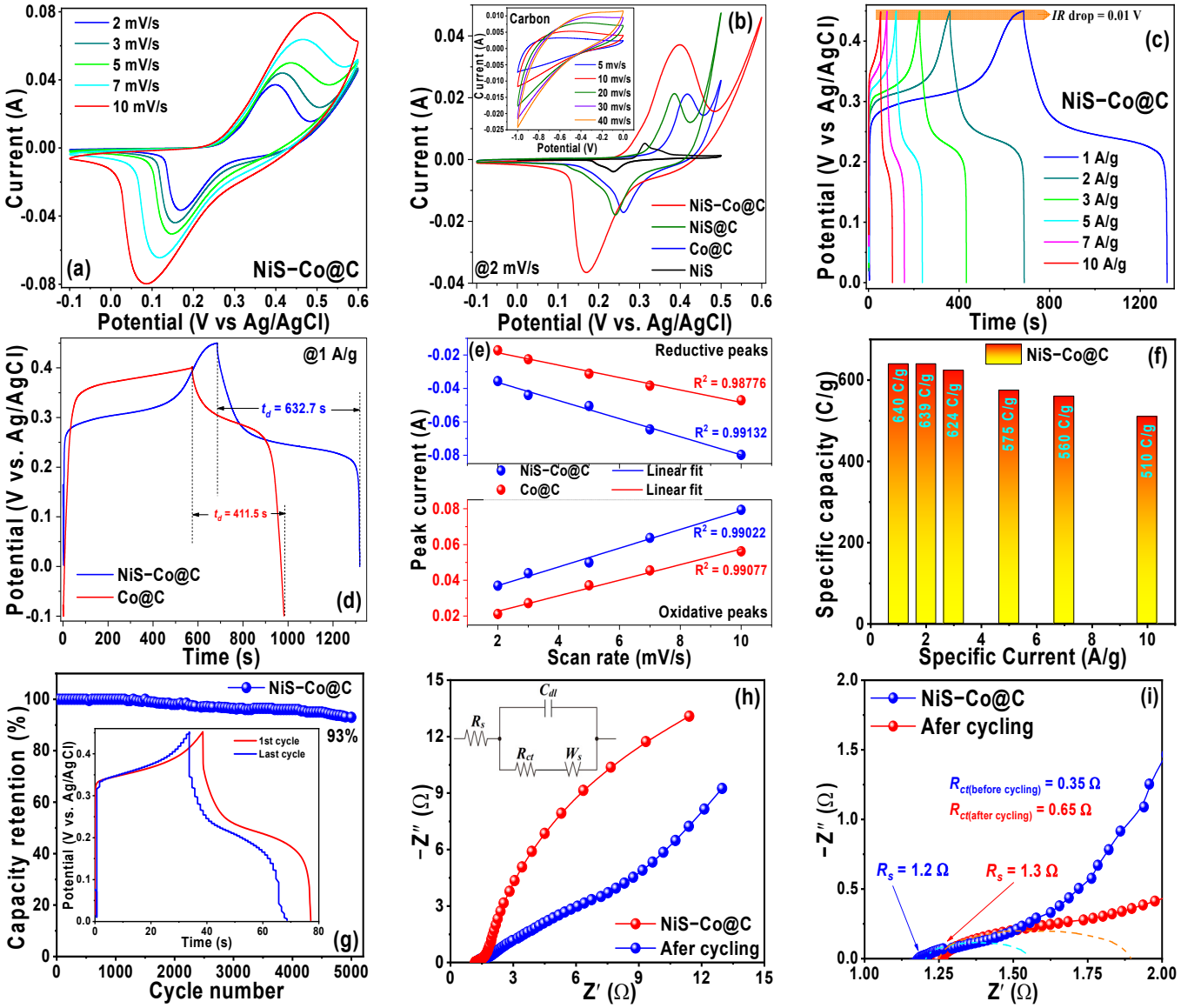

Figure 3. (**a**) CV of NiS-Co@C at different scan rates, (**b**) comparison of the CV between NiS-Co@C, NiS@C, Co@C, and NiS electrodes (inset: CV for the carbon matrix), (**c**) GCD of NiS-Co@C at different specific currents, (**d**) comparison of the GCD between NiS-Co@C and Co@C electrodes, (**e**) variation of peak currents against scan rates, (**f**) determination of specific capacity at different specific currents, (**g**) cyclic stability test of the NiS-Co@C electrode (inset: 1st and 5000th GCD cycles), (**h**) Nyquist plots of the NiS-Co@C electrode before and after the stability test (inset: equivalent circuit), and (**i**) high-frequency intercept of the Nyquist plots and the real impedance axis.

The broadness of the peaks suggests that the Co^{2+}/Co^{3+} and Co^{3+}/Co^{4+} conversions may also occur, as shown in the following equations [39]:

$$Co(OH)_2 + OH^- \leftrightarrow CoOOH + H_2O + e^- \quad (2a)$$

$$CoOOH + OH^- \leftrightarrow CoO_2 + H_2O + e^- \quad (2b)$$

In contrast, the Co@C electrode's redox peaks only correspond to the redox processes described in Equation (2a,b). As the scan rate increases, the CV curves show that the sharp redox peaks broaden. This behavior suggests that, at higher scan rates, the rapid processes limit the diffusion of electrolyte ions to the electrode's inner electroactive sites, leading to restricted redox activity. This observation implies that the electrochemical process is quasi-reversible, which is thermodynamically common for most practical electrochemical systems.

In addition to the strong redox peaks, the quasi-rectangular shapes of the CV curves for both the electrodes also indicate the presence of some capacitive-type surface-controlled process as the secondary mechanism. This is due to the presence of a carbon matrix within the ternary NiS-Co@C and binary Co@C electrodes, which facilitates the electric double-layer capacitive (EDLC) behavior as well [40]. Additionally, as depicted in the SEM images (see Figure 2a–f), the presence of Co and NiS nanoparticles at the surface of the carbon matrix manifests some surface pseudocapacitance (PC) as well, making the electrochemical process a combination of diffusion-controlled battery-like and surface-controlled capacitive-like mechanisms (EDLC + PC).

3.2.2. GCD Analysis

The GCD studies are conducted across a potential range from 0 to 0.5 V for both NiS-Co@C and Co@C electrodes to investigate the energy storage mechanisms at various specific currents, as shown in Figure 3c and Figure S3b, respectively. The distinct non-linear charge/discharge profiles with extended plateaus and rapid drops clearly highlight dominant battery-like behavior, along with secondary capacitive behavior, confirming the findings from the CV data. Additionally, the observed *IR* drops for both electrodes are minimal—0.01 V for NiS-Co@C and 0.016 V for Co@C—suggesting minimal interfacial resistance at the electrolyte/active material and active material/current collector junctions. The GCD performance at a specific current of 1 A/g is compared in Figure 3d, revealing that the NiS-Co@C electrode exhibits a significantly longer discharge time (t_d = 632.7 s) compared to the Co@C electrode (t_d = 411.5 s), demonstrating superior electrochemical performance and supporting the CV results. As noted earlier, from the CV data, the NiS-Co@C electrode's diverse oxidation states of Ni/Co, sulfur defects, and increased voids/pores facilitate better electrolyte ion diffusion within its nanostructure, enhancing redox activity and promoting better battery-type, diffusion-controlled electrochemical behavior compared to the Co@C electrode. It is known that the diffusion-controlled mechanism is more prominent at lower specific currents (also at lower scan rates) due to the slow nature of ion diffusion within the electrode's pores. At higher specific currents (and scan rates), ion diffusion is disrupted, and charge transfer primarily occurs at the surface, shifting to a surface-controlled process. However, a comparison of the GCD curves for both electrodes at 10 A/g (shown in Figure S3c) shows that the discharge time for the NiS-Co@C electrode (t_d = 51.89 s) is almost twice as long as that of the Co@C electrode (t_d = 25.06 s). Similarly, a comparison of the CV curves for both the electrodes @10 mV/s (cf. Figure S3d) reveals a much larger integral area of the NiS-Co@C electrode against Co@C. This indicates that the NiS-Co@C electrode's large pore and void structures allow the diffusion-controlled mechanism to remain active at higher specific currents (scan rates) as well, thus promoting dominant battery-type behavior. This further validates the quasi-reversible electrochemical mechanism in both electrodes, as previously discussed [19,38].

3.2.3. Analysis of Electrochemical Process

To understand the various electrochemical mechanisms, firstly, variations of the peak anodic current (I_{pa}), peak cathodic current (I_{pc}), and peak-to-peak separation potential ($\Delta E_{p\text{-}p} = E_{pa} - E_{pc}$, where E_{pa}/E_{pc} = anodic/cathodic peak potential) as a function of the scan rate are investigated for both the electrodes, and they are presented in Figure 3e and Figure S3e, respectively. The linear variations of I_{pa}, I_{pc}, and $\Delta E_{p\text{-}p}$ with respect to the scan rate indicate quasi-reversible electrochemical processes. Furthermore, both the I_{pa}/I_{pc} ratio and the formal potential ($E^{0'}$) are observed to be dependent on the scan rate. In an ideal reversible process, these parameters would remain unaffected by the

scan rate. For instance, the I_{pa}/I_{pc} ratio should equal 1, and the $E^{0'}$ should be the average of E_{pa} and E_{pc} in a reversible process [41].

Next, the specific capacity (C/g) and specific capacitance (F/g) of both the electrodes, influenced by their dominant battery-type behavior combined with secondary EDLC + PC-type contributions, are calculated using Equations (S1) and (S2) and are illustrated in Figure 3f and Figure S3f, respectively. At a specific current of 1.0 A/g, the NiS-Co@C electrode exhibits an exceptionally high specific capacity (capacitance) of 640 C/g (1488 F/g), compared to 492 C/g (1246 F/g) for the Co@C electrode. This trend persists across various specific currents, with capacity values of 639/480 C/g, 624/436 C/g, 575/396 C/g, 560/288 C/g, and 510/270 C/g for NiS-Co@C/Co@C electrodes at 2 (2), 3 (4), 5 (6), 7 (8), and 10 (10) A/g, respectively, thus corroborating the CV and GCD data, the reason of which was discussed earlier. Furthermore, the specific capacity decreases as the specific current increases, primarily due to diffusion limitations, as previously discussed. At elevated specific currents, the fast charge–discharge processes limit the diffusion of electrolyte ions into the material's core. Conversely, at lower specific currents, the extended penetration time enables more effective utilization of the active material, leading to a higher specific capacity.

To better understand the electrochemical performance and charge–transfer mechanism, the power law was applied to the CV data:

$$i_p(\nu) = a\nu^b \tag{3}$$

where i_p (A) represents the peak current, ν (mV/s) is the scan rate, and a and b are adjustable parameters. The exponent b typically falls between 0.5 and 1, where $b = 0.5$ signifies a diffusion-controlled process, and $b = 1$ indicates a surface-controlled charge storage mechanism. A b-value between these two extremes suggests a combination of both diffusion and surface contributions. Figure S3g,h presents the $\log(i_p)$ vs. $\log(\nu)$ plots for the NiS-Co@C and Co@C electrodes, respectively revealing a linear trend with b-values of approximately 0.52~0.54 and 0.61~0.63 for the reduction and oxidation peaks. This implies that charge storage is primarily diffusion-controlled with a secondary surface-controlled contribution. To further quantify the contributions of these mechanisms, Cottrell's equation was employed [42]:

$$i_p(\nu) = k_1\nu + k_2\nu^{1/2} \tag{4a}$$

which can be rewritten as:

$$i_p/\nu^{1/2} = k_1\nu^{1/2} + k_2 \tag{4b}$$

In this equation, $k_1\nu$ represents the surface-controlled charge storage, while $k_2\nu^{1/2}$ corresponds to the diffusion-controlled process. The values of k_1 and k_2 are determined from the slope and intercept of the linear fit. Figure S3i,k illustrates the plots of $i_p/\nu^{1/2}$ vs. $\nu^{1/2}$ for both electrodes, showing a linear correlation with extracted k_1/k_2 values of 0.73/26 ($\times 10^{-3}$) for NiS-Co@C and 1.6/12.9 ($\times 10^{-3}$) for Co@C. Figure S3j,l illustrates the proportional contributions of diffusion-controlled and surface-controlled charge storage at varying scan rates. Across all electrodes, the diffusion-controlled process dominates, aligning well with observations from CV and GCD analyses. However, it is noteworthy that, Equations (3) and (4) are primarily employed to analyze charge transfer dynamics, distinguishing between surface-controlled, diffusion-controlled, or a combination of both in an electrochemical process. It has not been used to interpret the electrochemical behavior as battery-like or capacitor-like as these mechanisms are interrelated and can occur simultaneously or in different proportions depending on the nature of the electrochemical reaction and the characteristics of the system, such as the material properties and the applied potential. Especially in advanced energy storage systems, surface-controlled mechanism can influence battery-type and capacitive-type behaviors since both rely on surface phenomena.

Likewise, the intercalation pseudocapacitance is associated with ion insertion/intercalation via diffusion, but it is accompanied by rapid redox reactions, which show characteristics of a capacitive behavior, such as quasi-rectangular CV curves with smaller redox peak humps and near-triangular GCD profiles with short plateau regions. Therefore, diffusion-controlled process is not necessarily always accompanied by battery-type electrochemical mechanism, whilst surface-controlled process can influence battery-type behavior too if ions cannot diffuse into the interior of the electrode quickly enough, especially at high rates. Therefore, to judge if the charge-storage mechanism is dominated by battery-type or capacitor-type (or a combination of both), the shape of the CV and GCD curves should be analyzed and compared properly. Typically, battery-like process involves well-separated, pronounced and sharp CV peaks (with minimal integral area), along with non-linear GCD profiles having long plateaus characterized by the sluggish diffusion-limited ion intercalation within the electrode's inner structure. In the current case, the *b*-value for the NiS-Co@C electrode is approximately 0.52–0.54, indicating a dominant diffusion-controlled process, which is consistent with the 92–96% diffusive contribution derived from Equation (4a,b). However, the CV curves of the NiS-Co@C electrode show well-separated, strong Faradaic redox peaks (with minimal integral area), accompanied by non-linear GCD profiles with long plateaus on the charge-discharge curves, indicating battery-type sluggish ion intercalation within the inner core of the electrode through diffusion. Based on these data, the electrochemical mechanism of the three-electrode system is interpreted as the dominant diffusion-controlled battery-type process [43–47].

Hence, as discussed earlier, several key factors contribute to the superior electrochemical performance of the NiS-Co@C electrodes: (1) *Primary Effect of Ion Intercalation and Battery-Type Behavior:* The abundant voids and nanopores in the nanosheet structure facilitate deep ion penetration, enabling a primarily diffusion-controlled, battery-like charge storage mechanism. (2) *Secondary Capacitive Contribution from the Carbon Matrix:* The conductive carbon framework supports an electric double-layer capacitance (EDLC) process, enhancing charge storage. (3) *Secondary Surface-Pseudocapacitance from Co Nanoparticles:* Surface-deposited Co nanoparticles introduce additional pseudocapacitive behavior in the NiS-Co@C electrode, promoting a secondary surface-controlled charge storage mechanism that further boosts electrochemical performance. (4) *Redox-Active Sites and Fast Charge Transfer:* The presence of abundant NiS nanoparticles provides multiple oxidation states and large number of defect centers, promotes numerous redox-active sites, and shortens ion diffusion pathways, facilitating rapid Faradaic reactions. (5) *Improved Charge Transport:* The Co@C matrix enhances electrical conductivity, optimizing charge transport across the electrode structure. These synergistic effects collectively lead to enhanced electrochemical properties of the NiS-Co@C electrode. A schematic representation of the charge storage mechanism is provided in Scheme 2.

For the Co@C electrode, its mainly the pseudocapacitive properties of Co and the EDLC behavior of the carbon matrix, coupled with optimized charge–transport properties of the Co@C base materials, that facilitate the electrochemical performance. Evidently, among the two electrodes, NiS-Co@C stands out as the superior performer, delivering a higher specific capacity. To further assess its stability, long-term cycling performance was evaluated over 5000 cycles at a specific current of 1 A/g, as shown in Figure 3g. Impressively, the electrode retained nearly 93% of its capacity, highlighting its outstanding rate capability and durability. The inset of Figure 3g shows the first and last GCD cycles, displaying near-identical curves with similar discharge times, further validating its outstanding long-term stability.

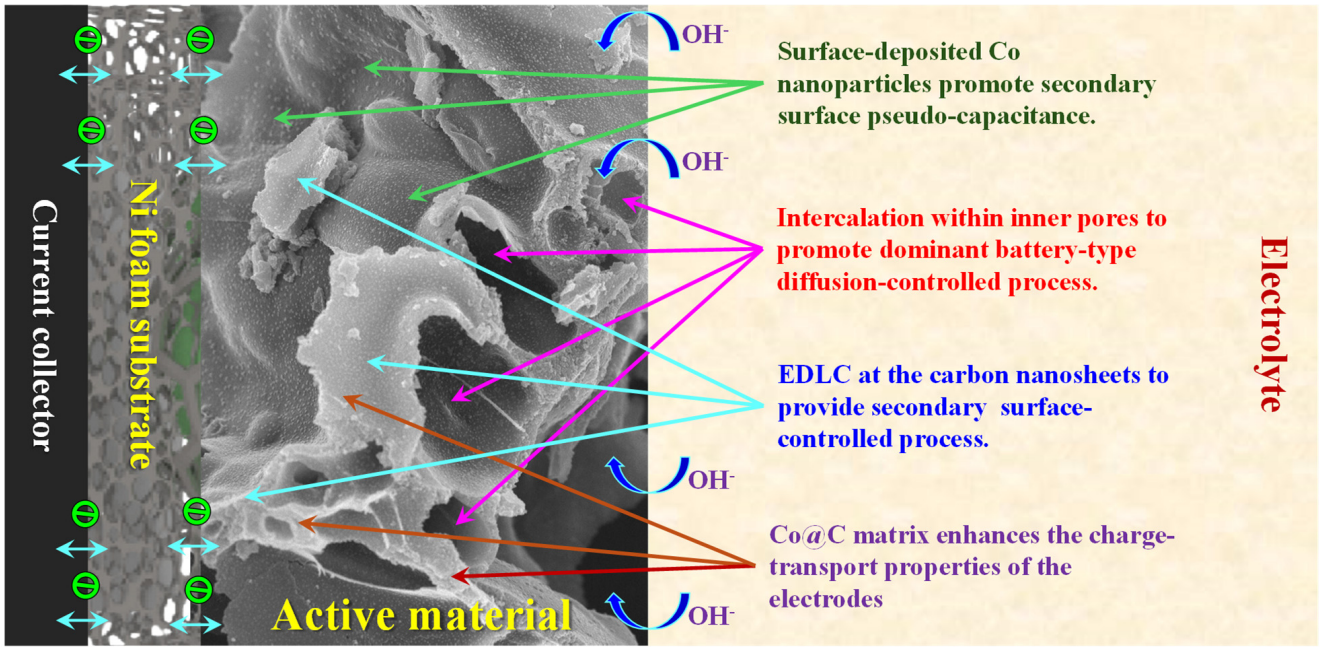

Scheme 2. Illustration of various charge storage mechanisms of the samples.

Additionally, the SEM images of the NiS-Co@C sample (at three magnifications) after the cycling test are shown in Figure S4a–c. The porous morphology of the surface with nanoparticle deposition is retained even after 5000 GCD cycles, indicating excellent structural integrity. However, some of the NiS nanoparticles are observed to be agglomerated, which, in general, reduces the grain-boundary scattering to improve charge transport properties. This is probably one of the reasons for 93% capacity retention over 5000 GCD cycles. To further corroborate this, XRD characterization is performed on the electrode after the cycling test, which is shown in Figure S4d. A comparison with the XRD curves of the fresh electrode (cf. Figure 1a) reveals only the presence of *fcc*-Co peaks. No NiS peaks are observed, indicating their amorphization, due to the local heat generation during long cycling. However, as indicated above, the reduction in the grain boundary scattering through the agglomeration of these nanoparticles probably compensated the increase in the resistivity of these particles due to amorphization, thus maintaining a balanced charge transport property over the entire 5000 GCD cycles.

As stated earlier, the enhanced electrochemical performance of NiS-Co@C compared to Co@C can be attributed to several key factors: (i) *Enhanced Redox Activity:* The presence of multiple oxidation states of Ni (Ni^{2+}/Ni^{3+}) and Co (Co^{2+}/Co^{3+}) facilitates more efficient redox reactions, improving charge storage capability. (ii) *Increased Electroactive Sites:* The higher BET surface area of NiS-Co@C results in an increased number of electroactive sites, while sulfur ions introduce a high density of defect centers, creating additional electroactive sites that reduce interfacial resistance and enhance charge transfer. (iii) *Optimized Ion Transport:* Compared to the Co@C electrode, the NiS-Co@C nanosheets feature a greater abundance of voids and pores, which shorten ion diffusion pathways and improve overall electrochemical performance. These structural and compositional advantages collectively contribute to the superior capacity retention and charge storage efficiency of the NiS-Co@C electrode.

Notably, the electrochemical properties of the NiS-Co@C electrode surpass those reported for similar electrodes under comparable conditions, as detailed in Table S2. Previous studies primarily reported specific capacitance (F/g), as they identified a surface-controlled charge storage mechanism (double-layer and pseudocapacitive), which enhances specific

power. In contrast, our study focuses on specific capacity (C/g) due to the observed combination of battery-type and EDLC + pseudocapacitive mechanisms, resulting in improved specific energy and power, as discussed later. Particularly, the current electrode depicts remarkable cyclic stability over large cycling against reported values, indicating that the binary metal-incorporated graphitic carbon matrix provides the required structural stability and buffers the volume expansion during cycling to considerably enhance the long-term durability and rate performance of the ternary NiS-Co@C electrochemical electrode.

3.2.4. EIS Analysis

Electrochemical impedance spectroscopy (EIS) measurements were conducted to gain deeper insights into the electrochemical kinetics, and the corresponding Nyquist plots for the NiS-Co@C electrode, both before and after cycling, are presented in Figure 3h. The equivalent series resistance (R_s), representing the solution contact resistance, is determined from the high-frequency intercepts on the real impedance axis in Figure 3i. The measured R_s values, ranging between 1.2 and 1.3 Ω, indicate minimal electrolyte resistance and low interfacial contact resistance between the electrode and electrolyte. The presence of suppressed semicircles in the mid-to-high-frequency region corresponds to charge-transfer resistance (R_{ct}), which arises due to electron transfer at the electrode–electrolyte interface. By analyzing the diameter of these semicircles, R_{ct} values of 0.35 Ω (for the fresh electrode) and 0.65 Ω (after cycling) were obtained, demonstrating remarkably low charge-transfer resistance even after prolonged use. In the low-frequency region, both fresh and cycled electrodes exhibit a nearly linear trend, with a slope of approximately 65–75° relative to the real impedance axis. This characteristic slope suggests that the electrochemical kinetics are primarily governed by diffusion-controlled processes. An equivalent circuit model, derived from the EIS data, is illustrated in the inset of Figure 3h, which is a parallel combination of charge-transfer resistance (R_{ct}) + Warburg impedance (W_s) and double-layer capacitance (C_{dl}), followed by a series connection with solution resistance (R_s). The significance of R_{ct} and R_s was already discussed. C_{dl} and W_s arise from the linear portion of the Nyquist plots at the mid-to-low frequency region. As stated, the slope of 65–75°, with respect to the Z' axis, indicates the presence of both capacitive as well as diffusion-limited processes, with C_{dl} rising from the EDLC mechanism of the binary Co@C matrix, while W_s emerges from the diffusion resistance within the ternary NiS-Co@C nanocomposite. These impedance results align well with the findings from CV and GCD analyses, further confirming the electrode's excellent charge storage properties [48–56].

3.3. Electrochemical Properties of a Two-Electrode Device (NiS-Co@C//AC)

Owing to the superior integration of battery-like and capacitor-like charge storage mechanisms, which provide high capacity, exceptional rate performance, and enhanced stability of the NiS-Co@C electrode, a high-efficiency two-electrode hybrid supercapacitor cell (HSC) is designed, with NiS-Co@C as the positive electrode and activated carbon (AC) as the negative electrode (NiS-Co@C//AC) for real-world charge storage applications. The schematic diagram of this configuration is shown in Figure 4a. This device is subjected to CV, GCD, EIS, and energy–power analysis to evaluate its performance and practical applicability.

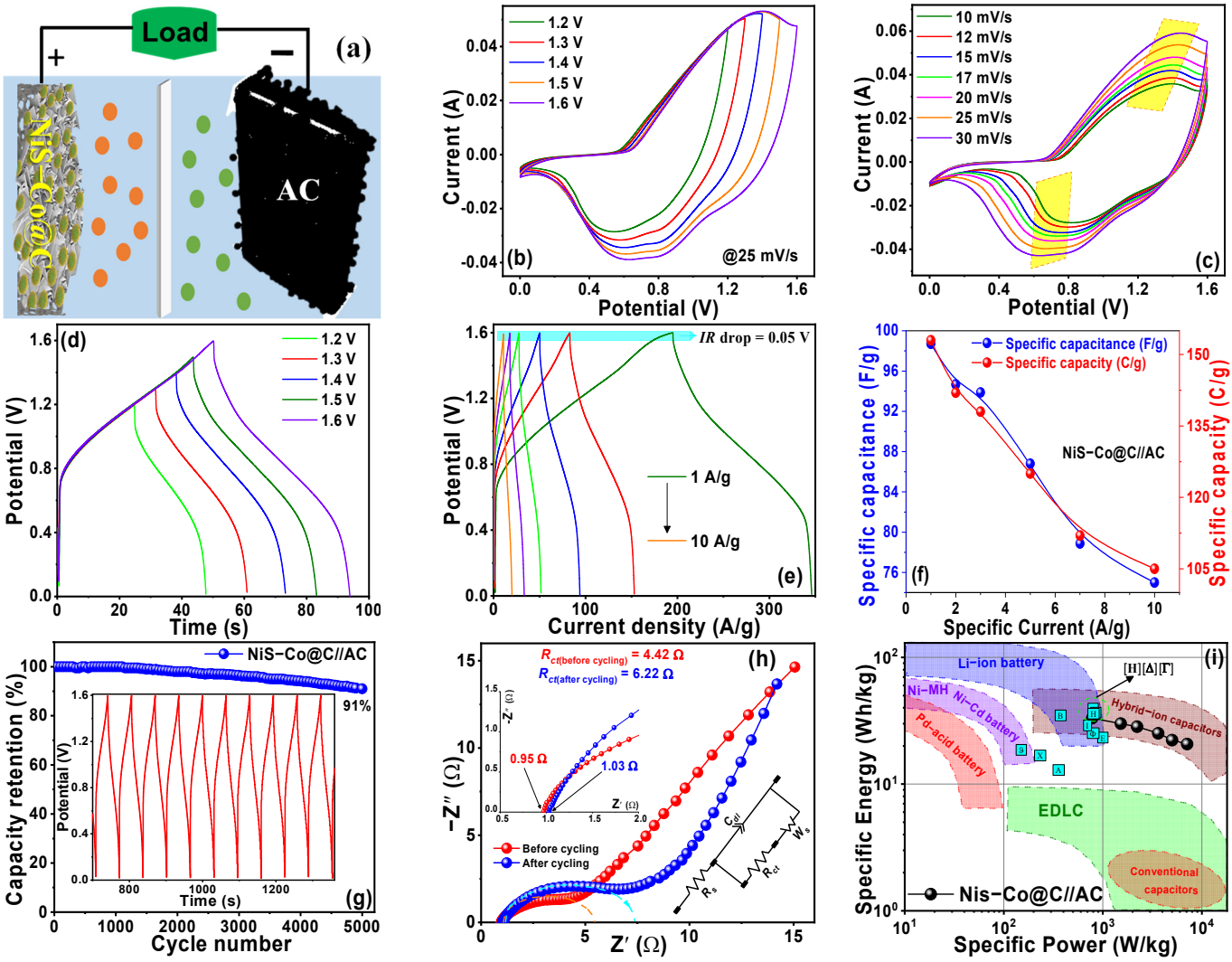

Figure 4. (**a**) Schematic representation of the NiS-Co@C//AC hybrid supercapattery device, (**b**) CV curves across different voltage windows, (**c**) CV curves at varying scan rates, (**d**) GCD curves for different voltage windows, (**e**) GCD curves at various specific currents, (**f**) specific capacitance as a function of specific current, (**g**) cyclic stability performance (inset: final ten GCD cycles), and (**h**) Nyquist plots (insets: enlarged view of high-frequency intercepts and the corresponding equivalent circuit), (**i**) Ragone plot, along with the energy–power fields of some conventional batteries and charge storage devices, and energy–power values of some reported similar devices (θ-[14], I-[20], H-[22], Γ-[35], Φ-[42], E-[48], Δ-[52], X-[53], B-[54], A-[56]).

3.3.1. CV Analysis of the Device

To determine the operational voltage range of the device, cyclic voltammetry (CV) measurements were performed across a range of working voltages from 1.2 V to 1.6 V (see Figure 4b), with no distortion observed in the resulting curves. This indicates that hydrogen and oxygen evolution reactions do not occur at the positrode and negatrode, allowing the maximum operating voltage window to be extended up to 1.6 V. Consequently, CV measurements were conducted at various scan rates within this 1.6 V voltage window, as shown in Figure 4c. The clearly defined, broad redox peaks in the CV curves, which maintain a consistent quasi-rectangular shape across different scan rates, highlight the combined effects of dominant battery-type behavior from the NiS-Co@C positive electrode and electric double-layer capacitance (EDLC) behavior from the activated carbon (AC) negative electrode. This demonstrates the HSC device's excellent rate capability and reversibility.

To gain deeper insights into the charge storage mechanism, *b*-fitting values were calculated using Equation (3) for the two-electrode system. As shown in Figure S5a, the NiS-Co@C//AC system yields a calculated *b*-value around 0.6–0.71. This result suggests a combination of diffusion-controlled and surface-controlled behaviors. This conclusion is further supported by CV curve analysis using a simulation method based on Cottrell's model (Equation (4)), which aligns with the experimental data. Figure S5b presents the k_1 and k_2 values from the oxidation and reduction peaks, which were used to calculate the contributions from the surface and diffusion processes. The corresponding relative contributions are shown in Figure S5c. As illustrated, the diffusive contributions range from 69% at a scan rate of 10 mV/s to 56% at 30 mV/s, further confirming the mixed-controlled process. Additionally, the fitted data were compared with experimental values in Figure S5d–f for three different scan rates, clearly indicating the combination of diffusion-controlled and surface-controlled processes, thus confirming a mixed-control mechanism.

However, as previously noted, since Equations (3) and (4) should not be interpreted in terms of battery-type or capacitor-type mechanisms, the hybrid supercapattery behavior of the device is analyzed based on the characteristics of the individual electrodes obtained from the three-electrode system and then compared with the CV and GCD profiles of the two-electrode device. It is evident that the dominant battery-type behavior of the NiS-Co@C positive electrode (characterized by strong redox peaks with minimal integral area in CV profiles, as shown in Figure 3a, and nonlinear GCD profiles with extended plateaus, as seen in Figure 3b) and the EDLC behavior of the carbon negative electrode (characterized by near-rectangular CV curves and triangular GCD profiles) are combined in the two-electrode system, resulting in quasi-rectangular CV curves with well-resolved redox peaks (cf. Figure 4c) and nonlinear GCD profiles with long plateaus (cf. Figure 4e). This suggests a hybrid mechanism involving both the redox-controlled, diffusion-driven battery-type process in the NiS-Co@C positive electrode and the surface-controlled, capacitive EDLC process in the AC negative electrode, thereby reinforcing the hybrid supercapattery behavior of the device. Therefore, the classification of the device as a supercapattery is supported by the combination of the battery-type and the capacitor-type processes, confirming the unique hybrid supercapattery mechanism [43–47].

3.3.2. GCD Analysis of the Device

GCD measurements were carried out across a range of operating voltages (1.2 to 1.6 V), revealing undistorted charge–discharge curves up to an optimal voltage of 1.6 V, which is consistent with the CV results (see Figure 4d). Based on these findings, further GCD analysis was conducted at varying specific currents within this 1.6 V working window (see Figure 4e). The resulting curves exhibit a distinct non-linear profile with slower voltage variation followed by rapid voltage drop along with prolonged charge-discharge durations, indicative of a hybrid battery–supercapacitor behavior. This indicates a substantial charge storage capacity and exceptional reversibility. Moreover, the device demonstrates minimal *IR* drop (0.05 V), signifying low interfacial resistance. Specific capacity (capacitance) values, derived from the GCD data, are plotted against specific currents in Figure 4f. At 1, 2, 3, 5, 7, 1, and 10 A/g, the specific capacity (capacitance) values are 153 C/g (99 F/g), 142 C/g (95 F/g), 138 C/g (94 F/g), 125 C/g (87 F/g), 112 C/g (79 F/g), and 105 C/g (75 F/g), respectively, highlighting its strong rate capability. The device also exhibits outstanding cycling stability, retaining 91.0% of its initial capacitance after 5000 GCD cycles (see Figure 4g). Additionally, the inset of Figure 4g presents the last 10 GCD cycles, showcasing undistorted curves that further confirm its exceptional long-term stability. The NiS-Co@C positrode, with its battery-like advantages (fast and deep ion intercalation/penetration, significant redox activity, rapid charge transfer at the electrode–electrolyte interface, and enhanced charge

transport between the active material and current collector), combined with the capacitor-like properties of the activated carbon negatrode (featuring a hierarchical porous structure, high thermal and chemical stability, outstanding electronic conductivity, and a broad operating temperature range), results in the exceptional electrochemical performance of the NiS-Co@C//AC supercapattery device.

3.3.3. EIS Analysis of the Device

The electrochemical impedance spectroscopy (EIS) analysis, represented by Nyquist plots in Figure 4h, compares the device's impedance response during the 1st and 5000th cycles. The nearly unchanged and low values of the equivalent series resistance or solution resistance (R_s ~ 0.95–1.03 Ω, calculated from the high-frequency intercept at the Z' axis, as shown at the inset of Figure 4h), which is the combination of the electrolyte resistance (between the electrodes), electrode–current collector interfacial resistance, and the internal resistance of the active material, reaffirm its exceptional charge transport properties and extraordinary cyclic stability. Furthermore, both plots exhibit a depressed semicircle in the high-to-mid-frequency region, indicative of charge transfer dynamics at the electrode-electrolyte interfaces. The charge transfer resistance (R_{ct}), estimated from the semicircle's diameter, remains relatively stable, approximately 4.42 Ω for the fresh electrode and 6.22 Ω after 5000 cycles. This minimal increase underscores the robustness of the active material and its efficient charge transport properties, which collectively contribute to the exceptional efficiency of the hybrid supercapattery. At the mid-to-low-frequency region, a linear tail is observed with an angle of 60–70° with the real impedance (Z') axis, indicating a combination of dominant diffusion-controlled processes (influenced by diffusion resistance of the NiS-Co@C positrode, often described by Warburg impedance, W_s) and capacitive processes (mostly controlled by the double-layer capacitance, C_{dl} of the AC negatrode), typical of a supercapattery mechanism, thus substantiating the CV and GCD results. Based on the EIS data, an equivalent circuit of the device is presented at the inset of Figure 4h.

3.3.4. Energy–Power Performance of the Device

The energy–power characteristics of the hybrid supercapattery are depicted in the Ragone plot (Figure 4i), demonstrating its impressive performance. The device achieves a peak specific energy of 33.15 Wh/kg at a specific power of 0.78 kW/kg. Even at a high power output of 7.1 kW/kg, it retains a specific energy of approximately 21 Wh/kg, marking an ~810% increase in power with only a ~37% reduction in energy. Additionally, as shown in the plot, these values are comparable or better than the reported values of similar asymmetric and hybrid energy storage devices [14,20,22,35,42,48,52–56]. A key highlight of this work is the device's exceptional cyclic stability, maintaining over 91–93%% capacity retention in both three-electrode (Table S2) and two-electrode configurations. This high stability is crucial for practical applications, as supercapatteries are often used in systems requiring frequent charge–discharge cycles, such as hybrid energy storage, electric vehicles, and renewable energy integration. Without sustained cyclic stability, performance degradation over time would lead to reduced efficiency, shorter lifespan, and increased maintenance costs. Ensuring long-term reliability and consistent energy output is therefore critical for their viability in real-world applications.

Figure 4i further compares the device's energy–power characteristics with various energy storage technologies, including Li-ion, Ni-MH, Ni-Cd, and Pb-acid batteries, as well as EDLCs, conventional capacitors, and hybrid-ion capacitors. The results show that this device outperforms EDLCs and conventional capacitors in energy–power performance, with specific energy comparable to the lower range of Li-ion batteries while matching or exceeding commercial batteries, such as Ni-MH, Ni-Cd, and Pb-acid. Additionally, its spe-

cific power surpasses most traditional batteries and aligns with hybrid-ion capacitors like Li-ion, Na-ion, and K-ion capacitors. This positioning makes it a strong contender for next-generation energy storage solutions, combining the high power delivery of supercapacitors with the substantial energy capacity of metal-ion batteries.

To demonstrate its practical potential, two solid-state pouch cells were wired in series to obtain a working voltage of 3.5 V. This setup successfully powered a 3 mm high-density red LED light (1.6 V, 20 mA) and an orange LED light (3.2 V, 18 mA) for an extended duration (see Figure 5a,b), further showcasing the device's robust energy storage capabilities.

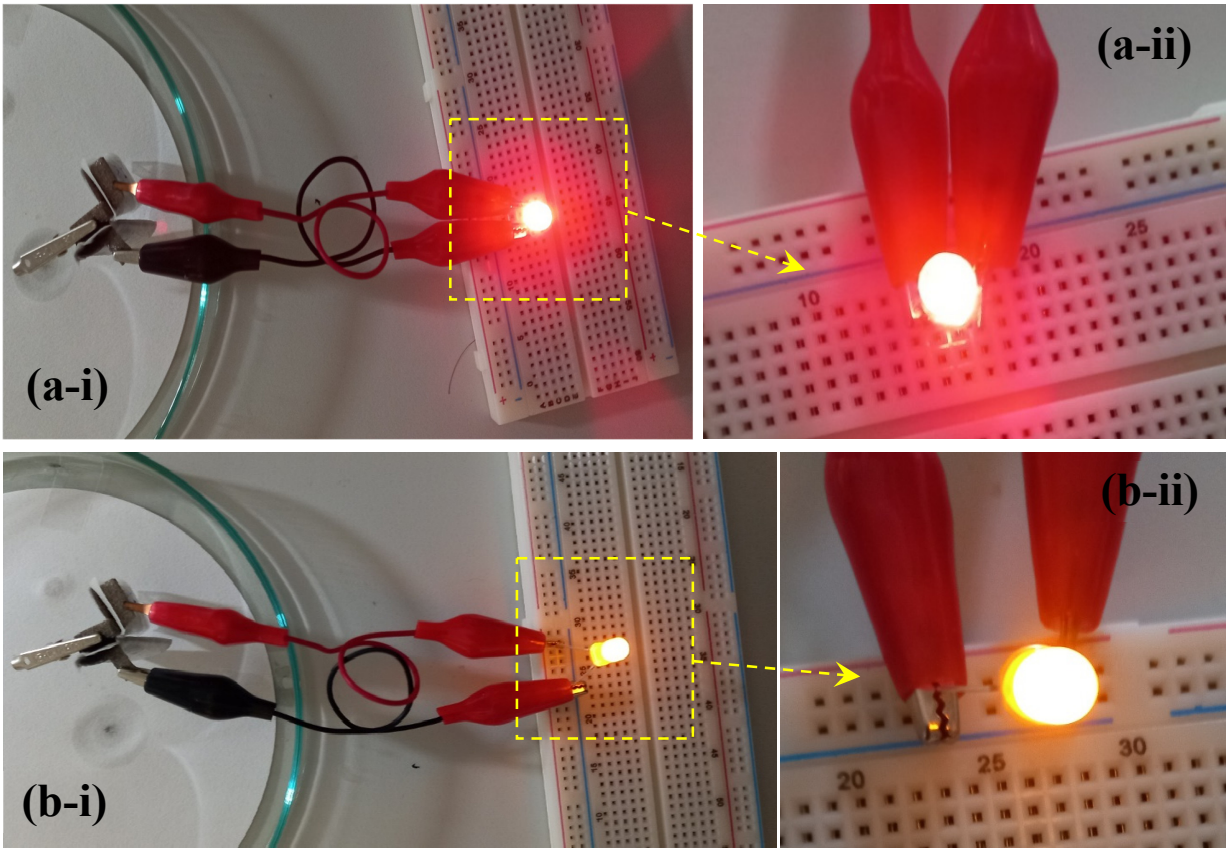

Figure 5. (**a-i**) Illumination of a red LED by series-connected pouch-cell type hybrid supercapattery device, (**a-ii**) close-up view, (**b-i**) illumination of an orange LED, (**b-ii**) close-up view.

4. Conclusions and Future Prospects

In this study, the ternary NiS-Co@C nanocomposite, synthesized through a pyrolysis–hydrothermal process using biomass, was designed as a hierarchical, highly crystalline nanosheet structure and was utilized as the electrode material in a hybrid supercapattery device. This innovative nanocomposite exhibited an impressive specific capacity of 640 C g^{-1} at a specific current of 1 A g^{-1}, coupled with exceptional cycling stability, maintaining 93% of its initial capacity after 5000 charge–discharge cycles. The incorporation of sulfur into the composite facilitates the generation of additional redox-active sites, thereby enhancing electrochemical performance. The Co@C framework significantly improves conductivity and structural integrity, which further contributes to better energy storage efficiency, charge transfer, and ion diffusion. In addition, the combination of the NiS-Co@C cathode with activated carbon (AC) as the anode resulted in a high-performance hybrid supercapattery, achieving a specific energy of 33 Wh kg^{-1} and maintaining 91% of its capacity over 5000 cycles. The synergistic interaction between the surface-controlled electric double-layer capacitance (EDLC) mechanism of AC and the diffusion-controlled battery-type behavior of NiS-Co@C enhances the energy

storage performance by introducing additional electroactive sites. This facilitates efficient electron and ion transfer, optimizes device stability and rate performance, and improves long-term cycling stability, ultimately increasing the overall charge storage capacity. This work presents a straightforward and controlled approach to design high-performance hybrid supercapattery electrodes, with the potential for scalable energy storage applications.

From a commercial perspective, while lithium-ion batteries (LIBs) currently dominate the energy storage sector, the need for cost-effective alternatives in large-scale applications—such as electric vehicles and power grids—coupled with concerns over the sustainability of lithium resources, has spurred the development of "beyond Li-ion" technologies [57–59]. Emerging alternatives, including alkali-ion batteries, Ni-MH, Ni-Cd, Pb-acid batteries, hybrid-ion capacitors, and asymmetric and hybrid supercapacitors [60–62], are gaining attention due to their cost advantages, particularly for applications where specific energy is less critical, such as grid load leveling. For instance, the cost of a typical LIB module is below USD 150/kWh, while these alternatives have demonstrated cost reductions exceeding 50%. An approximate cost calculation and comparison of the current device with an LIB module is presented in Supplementary Data S4, which estimates a nearly 1.5 to 3 times cost reduction against an LIB module. Given the use of low-cost, abundant materials and simple fabrication methods in this study, we anticipate that the cost of the developed device could be further reduced, making it a promising alternative to current energy storage solutions. Thus, the materials, devices, and technologies presented herein hold significant commercial potential for a wide range of applications in the energy storage sector.

Supplementary Materials: The following supporting information can be downloaded at: https://www.mdpi.com/article/10.3390/batteries11040116/s1, Physicochemical/Electrochemical characterizations, Device fabrication, N2 adsorption-desorption, and pore size distribution of Co@C sample, Table for XPS data, SEM-EDX data of Co@C, Electrochemical data for Co@C, SEM micrographs and XRD data of NiS-Co@C electrode after stability test, Tabular comparison of electrochemical data with literature values, Electrochemical data for NiS-Co@C//AC device, Approximate cost calculation and comparison of current device with an LIB module. References [63–75] are cited in the supplementary materials.

Author Contributions: Conceptualization, data curation, visualization, investigation, methodology, software, formal analysis, validation, writing—review and editing, M.R.P.; data curation, software, formal analysis, J.N.; supervision, investigation, data analysis, validation, software, writing—original draft, writing—review and editing, A.N.B.; funding acquisition, resources, project administration, S.-W.J. All authors have read and agreed to the published version of the manuscript.

Funding: The grant number 2019R1A5A8080290 of National Research Foundation of Korea (NRF) supports the funding for this study.

Data Availability Statement: The original contributions presented in the study are included in the article/Supplementary Materials, further inquiries can be directed to the corresponding author.

Conflicts of Interest: The authors declare no conflict of interest.

References

1. Dissanayaka, K.; Kularatna-Abeywardana, D. A review of supercapacitors: Materials, technology, challenges, and renewable energy applications. *J. Energy Storage* **2024**, *96*, 112563. [CrossRef]
2. Mendhe, A.; Panda, H.S. A review on electrolytes for supercapacitor device. *Discov. Mater.* **2023**, *3*, 29. [CrossRef]
3. Chatterjee, D.P.; Nandi, A.K. A review on the recent advances in hybrid supercapacitors. *J. Mater. Chem. A* **2021**, *9*, 15880–15918. [CrossRef]
4. Mandal, S.; Hu, J.; Shi, S.Q. A comprehensive review of hybrid supercapacitor from transition metal and industrial crop based activated carbon for energy storage applications. *Mater. Today Commun.* **2022**, *34*, 105207. [CrossRef]

5. Iqbal, M.Z.; Aziz, U. Supercapattery: Merging of battery-supercapacitor electrodes for hybrid energy storage devices. *J. Energy Storage* **2022**, *46*, 103823. [CrossRef]
6. Sivagurunathan, A.T.; Kavinkumar, T.; Seenivasan, S.; Kwon, Y.; Kim, D.-H. Enhancing high-performance supercapattery electrodes: Harnessing structural and compositional synergies via phosphorus doping on bimetallic boride for rapid charging. *J. Mater. Chem. A* **2023**, *11*, 20065–20078. [CrossRef]
7. Gao, D.; Luo, Z.; Liu, C.; Fan, S. A survey of hybrid energy devices based on supercapacitors. *Green Energy Environ.* **2023**, *8*, 972–988. [CrossRef]
8. Seenivasan, S.; Adhikari, S.; Sivagurunathan, A.T.; Kim, D.-H. Supercapatteries: Unlocking the potential of battery-supercapacitor fusion. *Energy Environ. Sci.* **2025**, *18*, 1054–1095. [CrossRef]
9. Rudra, S.; Seo, H.W.; Sarker, S.; Kim, D.M. Supercapatteries as Hybrid Electrochemical Energy Storage Devices: Current Status and Future Prospects. *Molecules* **2024**, *29*, 243. [CrossRef]
10. Liew, S.Q.; Jun, H.K. Fundamentals, Mechanism, and Materials for Hybrid Supercapacitors. In *Nanostructured Materials for Supercapacitors*; Thomas, S., Gueye, A.B., Gupta, R.K., Eds.; Springer International Publishing: Cham, Switzerland, 2022; pp. 71–100. [CrossRef]
11. Afif, A.; Rahman, S.M.; Azad, A.T.; Zaini, J.; Islan, A.; Azad, A.K. Advanced materials and technologies for hybrid supercapacitors for energy storage—A review. *J. Energy Storage* **2019**, *25*, 100852. [CrossRef]
12. Fan, W.; Wang, F.; Xiong, X.; Song, B.; Wang, T.; Cheng, X.; Zhu, Z.; He, J.; Liu, Y.; Wu, Y. Recent advances in functional materials and devices for Zn-Ion hybrid supercapacitors. *NPG Asia Mater.* **2024**, *16*, 18. [CrossRef]
13. Mahmoudi-Qashqay, S.; Zamani-Meymian, M.-R.; Maleki, A. A simple method of fabrication hybrid electrodes for supercapacitors. *Sci. Rep.* **2024**, *14*, 29105. [CrossRef] [PubMed]
14. Wang, H.; Liang, M.; Duan, D.; Shi, W.; Song, Y.; Sun, Z. Rose-like Ni3S4 as battery-type electrode for hybrid supercapacitor with excellent charge storage performance. *Chem. Eng. J.* **2018**, *350*, 523–533. [CrossRef]
15. Han, S.-C.; Kim, H.-S.; Song, M.-S.; Lee, P.S.; Lee, J.-Y.; Ahn, H.-J. Electrochemical properties of NiS as a cathode material for rechargeable lithium batteries prepared by mechanical alloying. *J. Alloys Compd.* **2003**, *349*, 290–296. [CrossRef]
16. Ondrejka, P.; Sojková, M.; Kotok, V.; Novák, P.; Hotovy, I.; Kemény, M.; Mikolášek, M. Tuning the electrochemical properties of NiS_2 2D-nanoflakes by one-zone sulfurization for supercapacitor applications. *Mater. Res. Express* **2023**, *10*, 065508. [CrossRef]
17. Yan, X.; Tong, X.; Ma, L.; Tian, Y.; Cai, Y.; Gong, C.; Zhang, M.; Liang, L. Synthesis of porous NiS nanoflake arrays by ion exchange reaction from NiO and their high performance supercapacitor properties. *Mater. Lett.* **2014**, *124*, 133–136. [CrossRef]
18. Wang, L.-H.; Ren, L.-L.; Qin, Y.-F.; Li, Q. Hydrothermal Preparation and High Electrochemical Performance of NiS Nanospheres as Anode for Lithium-Ion Batteries. *Front. Chem.* **2022**, *9*, 812274. [CrossRef]
19. Guan, Y.; Hu, K.; Su, N.; Zhang, G.; Han, Y.; An, M. Review of NiS-Based Electrode Nanomaterials for Supercapacitors. *Nanomaterials* **2023**, *13*, 979. [CrossRef]
20. Singh, D.; Samtham, M.; Bisht, N.; Choudhary, E.; Kumar, V.; Jangir, R.; Sonnathi, N.; Hosmani, S.S.; Katre, A.; Devan, R.S. Theoretical and experimental studies on 2D β-NiS battery-type electrodes for high-performance supercapacitor. *Electrochim. Acta* **2024**, *506*, 144998. [CrossRef]
21. Lee, Y.; Reddy, B.S.; Hong, H.; Kim, K.; Cho, S.; Ahn, H.; Ahn, J.; Cho, K. Synthesis and electrochemical properties of nickel sulfide/carbon composite as anode material for lithium-ion and sodium-ion batteries. *Int. J. Energy Res.* **2022**, *46*, 16883–16895. [CrossRef]
22. Ouyang, Y.; Chen, Y.; Peng, J.; Yang, J.; Wu, C.; Chang, B.; Guo, X.; Chen, G.; Luo, Z.; Wang, X. Nickel sulfide/activated carbon nanotubes nanocomposites as advanced electrode of high-performance aqueous asymmetric supercapacitors. *J. Alloys Compd.* **2021**, *885*, 160979. [CrossRef]
23. Yang, J.; Duan, X.; Guo, W.; Li, D.; Zhang, H.; Zheng, W. Electrochemical performances investigation of NiS/rGO composite as electrode material for supercapacitors. *Nano Energy* **2014**, *5*, 74–81. [CrossRef]
24. Wei, F.; Jiang, J.; Yu, G.; Sui, Y. A novel cobalt–carbon composite for the electrochemical supercapacitor electrode material. *Mater. Lett.* **2015**, *146*, 20–22. [CrossRef]
25. Kristl, M.; Dojer, B.; Gyergyek, S.; Kristl, J. Synthesis of nickel and cobalt sulfide nanoparticles using a low cost sonochemical method. *Heliyon* **2017**, *3*, e00273. [CrossRef] [PubMed]
26. Schmachtenberg, V.A.V.; Tontini, G.; Semione, G.D.L.; Drago, V. Nanostructured nickel sulfides synthesized by modified polyol method exhibiting blocking/freezing temperature. *J. Alloys Compd.* **2018**, *768*, 896–902. [CrossRef]
27. Lucchese, M.M.; Stavale, F.; Ferreira, E.H.M.; Vilani, C.; Moutinho, M.V.O.; Capaz, R.B.; Achete, C.A.; Jorio, A. Quantifying ion-induced defects and Raman relaxation length in graphene. *Carbon* **2010**, *48*, 1592–1597. [CrossRef]
28. Priya, B.A.; Sivakumar, T.; Parthibavarman, M.; Venkateswari, P. Design and fabrication of NiS decorating 2D ultra-thin TiO_2 thin film nanocomposites with enhanced photocatalytic hydrogen evolution activity. *J. Mater. Sci. Mater. Electron.* **2023**, *34*, 430. [CrossRef]

29. Artagan, Ö.; Vaizoğullar, A.İ.; Uğurlu, M. Activated carbon-supported NiS/CoS photocatalyst for degradation of methyl violet (MV) and selective disinfection process for different bacteria under visible light irradiation. *J. Taibah Univ. Sci.* **2021**, *15*, 154–169. [CrossRef]
30. Bishop, D.; Thomas, P.; Ray, A. Raman spectra of nickel(II) sulfide. *Mater. Res. Bull.* **1998**, *33*, 1303–1306. [CrossRef]
31. Dong, J.; Cheng, Z.; Zha, S.; Liu, M. Identification of nickel sulfides on Ni–YSZ cermet exposed to H_2 fuel containing H_2S using Raman spectroscopy. *J. Power Sources* **2006**, *156*, 461–465. [CrossRef]
32. Diallo, A.; Beye, A.; Doyle, T.; Park, E.; Maaza, M. Green synthesis of Co_3O_4nanoparticles via *Aspalathus linearis*: Physical properties. *Green Chem. Lett. Rev.* **2015**, *8*, 30–36. [CrossRef]
33. Galaburda, M.; Kovalska, E.; Hogan, B.T.; Baldycheva, A.; Nikolenko, A.; Dovbeshko, G.I.; Oranska, O.I.; Bogatyrov, V.M. Mechanochemical synthesis of carbon-stabilized Cu/C, Co/C and Ni/C nanocomposites with prolonged resistance to oxidation. *Sci. Rep.* **2019**, *9*, 17435. [CrossRef]
34. Leng, X.; Wei, S.; Jiang, Z.; Lian, J.; Wang, G.; Jiang, Q. Carbon-Encapsulated Co_3O_4 Nanoparticles as Anode Materials with Super Lithium Storage Performance. *Sci. Rep.* **2015**, *5*, 16629. [CrossRef]
35. Jiang, J.; Sun, Y.; Chen, Y.; Hu, X.; Zhu, L.; Chen, H.; Han, S. One-step synthesis of nickel cobalt sulfide nanostructure for high-performance supercapacitor. *J. Mater. Sci.* **2019**, *54*, 11936–11950. [CrossRef]
36. Morais, A.; Alves, J.P.C.; Lima, F.A.S.; Lira-Cantu, M.; Nogueira, A.F. Enhanced photovoltaic performance of inverted hybrid bulk-heterojunction solar cells using TiO2/reduced graphene oxide films as electron transport layers. *J. Photon Energy* **2015**, *5*, 057408. [CrossRef]
37. Choya, A.; de Rivas, B.; Gutiérrez-Ortiz, J.I.; González-Velasco, J.R.; López-Fonseca, R. Synthesis, Characterization and Kinetic Behavior of Supported Cobalt Catalysts for Oxidative after-Treatment of Methane Lean Mixtures. *Materials* **2019**, *12*, 3174. [CrossRef]
38. Chen, X.; Liu, Q.; Bai, T.; Wang, W.; He, F.; Ye, M. Nickel and cobalt sulfide-based nanostructured materials for electrochemical energy storage devices. *Chem. Eng. J.* **2021**, *409*, 127237. [CrossRef]
39. Naveen, A.N.; Selladurai, S. Investigation on physiochemical properties of Mn substituted spinel cobalt oxide for supercapacitor applications. *Electrochim. Acta* **2014**, *125*, 404–414. [CrossRef]
40. Ayaganov, Z.; Pavlenko, V.; Bin Haque, S.F.; Tanybayeva, A.; Ferraris, J.; Zakhidov, A.; Mansurov, Z.; Bakenov, Z.; Ng, A. A comprehensive study on effect of carbon nanomaterials as conductive additives in EDLCs. *J. Energy Storage* **2024**, *78*, 110035. [CrossRef]
41. Goswami, S.; Dillip, G.R.; Nandy, S.; Banerjee, A.N.; Pimentel, A.; Joo, S.W.; Martins, R.; Fortunato, E. Biowaste-derived carbon black applied to polyaniline-based high-performance supercapacitor microelectrodes: Sustainable materials for renewable energy applications. *Electrochim. Acta* **2019**, *316*, 202–218. [CrossRef]
42. Liu, T.; Zheng, Y.; Zhao, W.; Cui, L.; Liu, J. Uniform generation of NiCo2S4 with 3D honeycomb-like network structure on carbon cloth as advanced electrode materials for flexible supercapacitors. *J. Colloid Interface Sci.* **2019**, *556*, 743–752. [CrossRef] [PubMed]
43. Sharma, S.; Chand, P. Supercapacitor and electrochemical techniques: A brief review. *Results Chem.* **2023**, *5*, 100885. [CrossRef]
44. Liu, Y.; Jiang, S.; Shao, Z. Intercalation pseudocapacitance in electrochemical energy storage: Recent advances in fundamental understanding and materials development. *Mater. Today Adv.* **2020**, *7*, 100072. [CrossRef]
45. Brousse, T.; Bélanger, D.; Long, J.W. To Be or Not To Be Pseudocapacitive? *J. Electrochem. Soc.* **2015**, *162*, A5185–A5189. [CrossRef]
46. Forouzandeh, P.; Kumaravel, V.; Pillai, S.C. Electrode Materials for Supercapacitors: A Review of Recent Advances. *Catalysts* **2020**, *10*, 969. [CrossRef]
47. Ko, J.S.; Lai, C.-H.; Long, J.W.; Rolison, D.R.; Dunn, B.S.; Weker, J.N. Differentiating Double-Layer, Psuedocapacitance, and Battery-like Mechanisms by Analyzing Impedance Measurements in Three Dimensions. *ACS Appl. Mater. Interfaces* **2020**, *12*, 14071–14078. [CrossRef]
48. Kumar, S.; Sekar, S.; Kaliamurthy, A.K.; Lee, S. Bifunctional rGO-NiCo2S4 MOF hybrid with high electrochemical and catalytic activity for supercapacitor and nitroarene reduction. *J. Mater. Res. Technol.* **2021**, *12*, 2489–2501. [CrossRef]
49. Arumugam, P.; Sengodan, P.; Duraisamy, N.; Rajendran, R.; Vasudevan, V. An effective strategy to enhance the photocatalytic performance by forming NiS/rGO heterojunction nanocomposites. *Ionics* **2020**, *26*, 4201–4212. [CrossRef]
50. Zhao, J.; Wang, Y.; Qian, Y.; Jin, H.; Tang, X.; Huang, Z.; Lou, J.; Zhang, Q.; Lei, Y.; Wang, S. Hierarchical Design of Cross-Linked $NiCo_2S_4$ Nanowires Bridged NiCo-Hydrocarbonate Polyhedrons for High-Performance Asymmetric Supercapacitor. *Adv. Funct. Mater.* **2022**, *33*, 2210238. [CrossRef]
51. Chen, X.; Ding, B.; Sun, Y. Facile synthesis of $NiCo_2S_4$ nanosheets on graphitized carbon microspheres for high-performance asymmetric supercapacitors. *J. Energy Storage* **2021**, *35*, 102309. [CrossRef]
52. Cheng, M.; Fan, H.; Song, Y.; Cui, Y.; Wang, R. Interconnected hierarchical $NiCo_2O_4$ microspheres as high-performance electrode materials for supercapacitors. *Dalton Trans.* **2017**, *46*, 9201–9209. [CrossRef] [PubMed]
53. Xu, S.; Su, C.; Wang, T.; Ma, Y.; Hu, J.; Hu, J.; Hu, N.; Su, Y.; Zhang, Y.; Yang, Z. One-step electrodeposition of nickel cobalt sulfide nanosheets on Ni nanowire film for hybrid supercapacitor. *Electrochim. Acta* **2018**, *259*, 617–625. [CrossRef]

54. Su, S.; Sun, L.; Xie, F.; Qian, J.; Zhang, Y. Phosphorus-doped Ni-Co sulfides connected by carbon nanotubes for flexible hybrid supercapacitor. *Front. Chem. Sci. Eng.* **2023**, *17*, 491–503. [CrossRef]
55. Chen, W.; Xia, C.; Alshareef, H.N. One-Step Electrodeposited Nickel Cobalt Sulfide Nanosheet Arrays for High-Performance Asymmetric Supercapacitors. *ACS Nano* **2014**, *8*, 9531–9541. [CrossRef]
56. Chen, X.; Sun, M.; Jaber, F.; Nezhad, E.Z.; Hui, K.S.; Li, Z.; Bae, S.; Ding, M. A flexible wearable self-supporting hybrid supercapacitor device based on hierarchical nickel cobalt sulfide@C electrode. *Sci. Rep.* **2023**, *13*, 15555. [CrossRef]
57. Vedhanarayanan, B.; Lakshmi, K.C.S. Beyond lithium-ion: Emerging frontiers in next-generation battery technologies. *Front. Batter. Electrochem.* **2024**, *3*, 1377192. [CrossRef]
58. Banerjee, A.N.; Joo, S.W. 'Beyond Li-ion technology'—A status review. *Nanotechnology* **2024**, *35*, 472001. [CrossRef]
59. Au, H.; Crespo-Ribadeneyra, M.; Titirici, M.-M. Beyond Li-ion batteries: Performance, materials diversification, and sustainability. *One Earth* **2022**, *5*, 207–211. [CrossRef]
60. Patil, U.M.; Katkar, P.K.; Marje, S.J.; Lokhande, C.D.; Jun, S.C. Hydrous nickel sulphide nanoparticle decorated 3D graphene foam electrodes for enhanced supercapacitive performance of an asymmetric device. *New J. Chem.* **2018**, *42*, 20123–20130. [CrossRef]
61. Belekar, K.G.; Patil, S.S.; Bhosale, S.B.; Kumbhar, S.S.; Jadhav, G.D.; Parale, V.G.; Lokhande, C.D.; Park, H.-H.; Katkar, P.K.; Patil, U.M. Amorphous, binder-free cobalt manganese phosphate cathodes prepared by SILAR method for asymmetric supercapacitors: Harnessing cationic synergy. *Synth. Met.* **2024**, *311*, 117800. [CrossRef]
62. Katkar, P.K.; Lee, S.-W. An Interfacial Engineering Approach of Flower-like Li^+ Preintercalated Co–Cu Phosphate for Solid-State Hybrid Energy Storage Device. *ACS Sustain. Chem. Eng.* **2024**, *12*, 5927–5942. [CrossRef]
63. Sing, K.S.W. Reporting physisorption data for gas/solid systems with special reference to the determination of surface area and porosity. *Pure Appl. Chem.* **1985**, *57*, 603–619. [CrossRef]
64. Wang, T.; Xu, Z.; Yuan, K.; Wang, X.; Ge, M. Paleoenvironment and shale gas potential of the Carboniferous Dawuba and the Cambrian Niutitang shales in the Upper Yangtze Platform, South China. *Front. Earth Sci.* **2024**, *12*, 1404178. [CrossRef]
65. Nichterwitz, M.; Grätz, S.; Nickel, W.; Borchardt, L. Solvent-free hierarchization of zeolites by carbochlorination. *J. Mater. Chem. A* **2017**, *5*, 221–229. [CrossRef]
66. Hua, H.; Liu, S.; Chen, Z.; Bao, R.; Shi, Y.; Hou, L.; Pang, G.; Hui, K.N.; Zhang, X.; Yuan, C. Self-sacrifice template formation of hollow hetero-Ni_7S_6/Co_3S_4 nanoboxes with intriguing pseudo-capacitance for high-performance electrochemical capacitors. *Sci. Rep.* **2016**, *6*, 20973. [CrossRef]
67. Annamalai, K.P.; Liu, L.; Tao, Y. Highly exposed nickel cobalt sulfide–rGO nanoporous structures: An advanced energy-storage electrode material. *J. Mater. Chem. A* **2017**, *5*, 9991–9997. [CrossRef]
68. Abdul, S.K.; Anuj, K.; Amjad, F.; Mohammad, T.; Muhammad, A.; Muhammad, U.; Akmal, A.; Saira, A.; Lujun, P.; Ghulam, Y. Benchmarking the charge storage mechanism in nickel cobalt sulfide nanosheets anchored on carbon nanocoils/carbon nanotubes nano-hybrid for high performance supercapacitor electrode. *J. Energy Storage* **2022**, *56*, 106041. [CrossRef]
69. Xiong, X.; Jin, J.; Xie, M.; Chen, J.; Zhang, Y.; Wan, L.; Du, C. Cobalt-nickel sulfide hierarchical hollow microspheres to boost electrochemical activity for supercapacitors. *J. Alloys Compd.* **2024**, *1010*, 177730. [CrossRef]
70. Zhang, D.; Liu, H.; Xiao, Y.; Guo, L.; Wan, H. Yolk@shell layered NiCo hydroxide: Controllable synthesis, sulfuration and electrochemical applications for hybrid supercapacitors. *J. Alloys Compd.* **2025**, *1010*, 177187. [CrossRef]
71. Yu, H.; Shen, D.; Zhang, R.; Zhao, S. Synthesis of flower-like crystal nickel–cobalt sulfide and its supercapacitor performance. *Coatings* **2024**, *14*, 564. [CrossRef]
72. Kumar, Y.A.; Yadav, A.A.; Al-Asbahi, B.A.; Kang, S.-W.; Moniruzzaman, M. Sulfur nanoparticle-decorated nickel cobalt sulfide hetero-nanostructures with enhanced energy storage for high-performance supercapacitors. *Molecules* **2022**, *27*, 7458. [CrossRef] [PubMed]
73. Orangi, S.; Manjong, N.; Clos, D.P.; Usai, L.; Burheim, O.S.; Strømman, A.H. Historical and prospective lithium-ion battery cost trajectories from a bottom-up production modeling perspective. *J. Energy Storage* **2024**, *76*, 109800. [CrossRef]
74. Dura, H.; Perry, J.; Lecacou, T.; Markoulidis, F.; Lei, C.; Khalil, S.; Decker, M.; Weil, M. Cost analysis of supercapacitor cell production. In Proceedings of the 2013 International Conference on Clean Electrical Power (ICCEP), Alghero, Italy, 11–13 June 2013; pp. 516–523.
75. Qi, W.; Sathre, R.; Morrow, W.R., III; Shehabi, A. Unit Price Scaling Trends for Chemical Products, Ernest Orlando Lawrence Berkeley National Laboratory. August 2015. Available online: https://eta-publications.lbl.gov/sites/default/files/lbnl-189844.pdf (accessed on 18 March 2025).

Disclaimer/Publisher's Note: The statements, opinions and data contained in all publications are solely those of the individual author(s) and contributor(s) and not of MDPI and/or the editor(s). MDPI and/or the editor(s) disclaim responsibility for any injury to people or property resulting from any ideas, methods, instructions or products referred to in the content.